Asymmetric Tidal Mixing due to the Horizontal Density Gradient*

MING LI

Horn Point Laboratory, University of Maryland Center for Environmental Science, Cambridge, Maryland

JOHN TROWBRIDGE AND ROCKY GEYER

Department of Applied Ocean Physics and Engineering, Woods Hole Oceanographic Institution, Woods Hole, Massachusetts

(Manuscript received 7 June 2005, in final form 15 March 2007)

ABSTRACT

Stratification and turbulent mixing exhibit a flood–ebb tidal asymmetry in estuaries and continental shelf regions affected by horizontal density gradients. The authors use a large-eddy simulation (LES) model to investigate the penetration of a tidally driven bottom boundary layer into stratified water in the presence of a horizontal density gradient. Turbulence in the bottom boundary layer is driven by bottom stress during flood tides, with low-gradient (Ri) and flux (R_f) Richardson numbers, but by localized shear during ebb tides, with Ri = ¼ and R_f = 0.2 in the upper half of the boundary layer. If the water column is unstratified initially, the LES model reproduces periodic stratification associated with tidal straining. The model results show that the energetics criterion based on the competition between tidal straining and tidal stirring provides a good prediction for the onset of periodic stratification, but the tidally averaged horizontal Richardson number Ri_x has a threshold value of about 0.2, which is lower than the 3 suggested in a recent study. Although the tidal straining leads to negative buoyancy flux on flood tides, the authors find that for typical values of the horizontal density gradient and tidal currents in estuaries and shelf regions, buoyancy production is much smaller than shear production in generating turbulent kinetic energy.

1. Introduction

Tidal currents provide a major mechanism for generating turbulent mixing in estuaries and continental shelves. Recent observations have revealed significant asymmetry in turbulent mixing over a tidal cycle. Jay and Smith (1990) analyzed data collected from the Columbia River estuary and found a flood–ebb asymmetry: enhanced shear and stratification during ebb tides but stronger mixing and weaker stratification during flood tides. Nepf and Geyer (1996) investigated intratidal variations in boundary layer structure in a straight section of the Hudson River estuary. They found that active mixing with a gradient Richardson number less than ¼ is confined to a well-mixed nearbed layer on floods but occurs throughout regions of significant stratification on ebbs. More recently, Geyer et al. (2000) estimated eddy viscosity in the Hudson River and found that flood values exceeded ebb values by a factor of 2. Other estuarine field studies have also documented this tidal asymmetry and suggested that the asymmetric mixing needs to be considered when calculating tidally averaged vertical fluxes (e.g., Stacey et al. 2001). In addition to the flood–ebb asymmetry, turbulent mixing exhibits large fluctuations over the spring–neap cycle. For example, Peters (1999) found that all flood tides have substantial mixing but that spring ebbs have the strongest mixing extending throughout the water column.

In weakly stratified flows found in regions of the continental shelf influenced by lateral freshwater inputs (e.g., the Rhine outflow area of the North Sea and the Liverpool Bay), Simpson et al. (1990, hereafter S90) independently discovered the same phenomenon and described the switching between the stratified and mixed states over a single tidal cycle as strain-induced periodic stratification (SIPS). In the Liverpool Bay, Simpson et al. (2002) and Rippeth et al. (2001) found pronounced asymmetry in energy dissipation between the flood and ebb tidal regimes. During the ebb, the water column stratifies and strong dissipation is confined to the lower half of the water column. By contrast, during

* University of Maryland Center for Environmental Science Contribution Number 4107.

Corresponding author address: Ming Li, Horn Point Laboratory, University of Maryland Center for Environmental Science, P.O. Box 775, Cambridge, MD 21613.
E-mail: mingli@hpl.umces.edu

DOI: 10.1175/2007JPO3372.1

the flood, stratification is eroded with complete vertical mixing occurring at high water and higher values of dissipation extending throughout the water column.

These observations of asymmetric tidal mixing have motivated both theoretical and numerical investigations. In their original paper, S90 illustrated the tidal straining mechanism by which differential advection of a tidal current in the presence of a horizontal density gradient generates periodic stratification in an initially homogeneous water column. One-dimensional numerical models that incorporate turbulence closure schemes have been used to further illustrate the tidal straining mechanism. In particular, Simpson et al. (2002) employed a 1D k–ε turbulence closure model to explain the observed semidiurnal cycle of dissipation in a region of freshwater influence in the Irish Sea. The model produced a reasonable account of energy dissipation and its asymmetric behavior on ebb and flood. However, the model had difficulty in reproducing some observed features; for example, the maximum dissipation in the upper half of the water column was shorter in duration in the model.

Despite these interesting studies in recent years, several key questions on the flood–ebb tidal asymmetry remain unanswered. What are the relative roles of baroclinic pressure gradient and tidal straining in estuarine dynamics? Is the estuarine circulation driven by the baroclinic pressure gradient as hypothesized in the classic theory of Pritchard (1956) or is it driven by tidal straining and asymmetric tidal mixing as proposed in recent papers (e.g., Jay and Smith 1990; Stacey et al. 2001)? Is the flood–ebb mixing asymmetry caused by the flood–ebb asymmetry in the bed stress or is it caused by tidal straining of the density field? When examining density and current profiles collected in an estuarine channel in the San Francisco Bay, Stacey and Ralston (2005) found negative gradient Richardson numbers and unstable density profiles in the upper portions of the boundary layer during the flood tides. Based on these results, they suggested that the tidal asymmetry is due to the strain-induced buoyancy flux, which is stabilizing on ebb tides but destabilizing on flood tides. Do the flows switch from shear- to convective-driven turbulence over a tidal cycle for the observed range of the horizontal density gradient? How does the strain-induced buoyancy production compare with shear production in the turbulence kinetic energy (TKE) budget?

To gain insight into these questions, we use a large-eddy simulation (LES) model to simulate the tidally driven bottom boundary layer in both stratified and weakly stratified water. Low-level turbulence closure models only resolve the mean flows and rely on empirical schemes to parameterize higher-order terms. In contrast, LES models resolve both the mean flows and energy-containing turbulent eddies that dominate turbulent momentum and energy transports. LES models have been used to simulate turbulent large eddies in the upper ocean, yielding new insights that could not be obtained from the turbulence closure models (e.g., Skyllingstad et al. 1999; Li et al. 2005a). Because of high computational costs, LES is usually limited to small domain sizes and cannot resolve large-scale flows. Moreover, most LES models used in oceanic boundary layer studies assume periodic boundary conditions in the horizontal directions. To address the asymmetric tidal mixing in the presence of a horizontal density gradient, we shall generalize the LES equations by incorporating a large-scale pressure gradient in the momentum equation and a large-scale salinity advection in the salinity equation.

The small spatial scales of turbulent eddies and the anisotropy of the outer scales of flow make stratified turbulence a challenging problem to simulate numerically. The LES model can provide an accurate simulation of turbulent flows in the weakly stratified bottom boundary layer but may become inaccurate in the strongly stratified pycnocline region where the buoyancy length scale falls below the grid size. Despite these challenges, there has been recent progress in modeling the stratified flows with LES. Mason and Derbyshire (1990) and Brown et al. (1994) applied LES to stably stratified atmospheric boundary layers, while Skyllingstad et al. (1999) used LES to simulate the deepening of the ocean surface mixed layer into the stratified pycnocline during a westerly wind burst event. This paper is in the same spirit as these studies. While we recognize the limitations of the LES model in the strongly stratified region, we also believe that it provides a valuable approach that is complementary to the observations and turbulence closure models. For the weakly stratified flows found in regions of the continental shelf influenced by lateral freshwater inputs, the LES model does not suffer from the resolution issue and should be particularly useful for illuminating the physics of tidal straining in these flows.

The plan for the paper is as follows: in section 2 we shall derive the generalized LES equations; section 3 is devoted to a detailed investigation of turbulence dynamics in a partially mixed estuary; and section 4 examines the effects of tidal straining in weakly stratified environments such as shelf seas.

2. Generalized LES equations for horizontally inhomogeneous flows

Figure 1 shows a schematic diagram of a partially mixed estuary. Reynolds-averaged models (RANS)

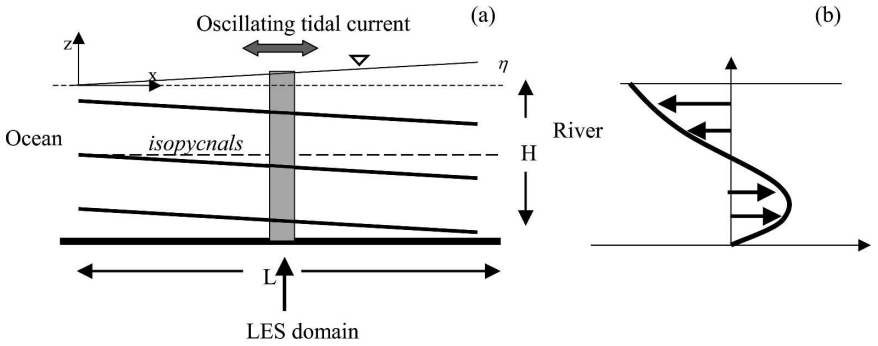

FIG. 1. A schematic diagram of a partially mixed estuary: (a) longitudinal isopycnal distribution and LES model domain and (b) baroclinic pressure gradient driving the two-layer estuarine circulation.

such as the Regional Ocean Modeling System (ROMS) resolve mean flows over an entire estuary but rely on turbulence closure schemes to parameterize turbulence effects. In contrast, LES uses fine resolution to resolve flux-carrying turbulent eddies, but its domain size is usually too small to resolve the large-scale flows. Therefore, we need to develop an approach for incorporating the effects of large-scale flows and gradients into the LES model.

Let us briefly review momentum and salt balance in a simple two-dimensional estuary. As shown in Fig. 1, freshwater inflow at the head of an estuary leads to a sea level slope directed toward the ocean, whereas sloping isopycnals result in a baroclinic pressure gradient directed landward. The along-stream momentum equation in the LES model needs to take this large-scale pressure gradient into account. For the salt balance in a partially mixed estuary, the principal balance is between horizontal advection $\overline{u}\partial\overline{S}/\partial x$ (where $\overline{u}$ is the mean velocity and $\partial\overline{S}/\partial x$ is the horizontal salinity gradient) and vertical turbulent flux. If the tidally averaged flow exhibits a two-layer residual circulation, then this horizontal advection builds up stratification in the water column, but turbulent diffusion reduces the vertical density difference.

To incorporate the effects of the horizontal density gradient, we generalize the LES equations to

$$\frac{\partial u}{\partial t} + \mathbf{u}\cdot\nabla u = -\frac{1}{\rho}\frac{\partial p}{\partial x} - \frac{1}{\rho}\frac{\partial p}{\partial x} + \text{SGS}, \tag{1}$$

$$\frac{\partial v}{\partial t} + \mathbf{u}\cdot\nabla v = -\frac{1}{\rho}\frac{\partial p}{\partial y} + \text{SGS}, \tag{2}$$

$$\frac{\partial w}{\partial t} + \mathbf{u}\cdot\nabla w = -g\frac{\rho'}{\rho} - \frac{1}{\rho}\frac{\partial p}{\partial z} + \text{SGS}, \tag{3}$$

$$\frac{\partial S}{\partial t} + \mathbf{u}\cdot\nabla S = -u\frac{\partial\overline{S}}{\partial x} + \text{SGS}, \tag{4}$$

where the longitudinal pressure gradient can be evaluated by making hydrostatic approximations for the large-scale flows:

$$-\frac{1}{\rho}\frac{\partial P}{\partial x} = F_{\text{tide}} - g\frac{\partial\eta}{\partial x} - \frac{g}{\rho_0}\int_z^\eta \frac{\partial\rho'}{\partial x}\,dz', \tag{5}$$

where the first term represents the barotropic forcing due to tidal currents. The tidal forcing can be specified as an oscillating body force $F_{\text{tide}} = (\partial U/\partial t)$ and $U = V_{\max}\sin(\omega_0 t)$, which has a maximum speed $V_{\max}$ and an M_2 tidal frequency ω_0 (e.g., Li et al. 2005b). The second term in (5) represents freshwater pileup at the river head, and the third term represents the baroclinic pressure gradient due to sloping isopycnals. Since the second and third terms on the right-hand side of Eq. (5) represent the nontidal pressure gradient driving the two-layer estuarine flow, their vertical integral should be zero. Hence the second term cannot be chosen arbitrarily [see, e.g., Eq. (16)]. One can think of these large-scale terms as forcing terms on the local turbulent flows simulated in LES. Simpson and Souza (1995) employed a similar generalization scheme to their 1D turbulence closure model. The subgrid-scale (SGS) terms are shown schematically in Eqs. (1)–(4).

Alternatively, we can derive Eqs. (1)–(4) using a multiscale expansion method as used in Wang et al. (1998). Let us denote (x, y, z) as the inner scale resolved by LES and $(\overline{x}, \overline{y}, \overline{z})$ as the outer scale resolved by a regional ocean model such as the ROMS. The total flow field can be decomposed by using a Taylor expansion with respect to the outer scale $\overline{x}$ in the longitudinal direction:

$$u_{\text{total}} = u(x, y, z, t) + \overline{x}\left(\frac{\partial\overline{u}}{\partial\overline{x}}\right)_z + \text{HOT}, \tag{6}$$

$$S_{\text{total}} = S(x, y, z, t) + \overline{x}\left(\frac{\partial\overline{S}}{\partial\overline{x}}\right)_z + \text{HOT}, \tag{7}$$

$$P_{\text{total}} = P(x, y, z, t) + \overline{x}\left(\frac{\partial\overline{P}}{\partial\overline{x}}\right)_z + \text{HOT}, \tag{8}$$

where HOT stands for higher-order terms. Substituting these expansions into the filtered Navier–Stokes equations and keeping the leading-order terms yields

$$\frac{\partial u}{\partial t} + \mathbf{u}\cdot\nabla u + u\frac{\partial \overline{u}}{\partial \overline{x}} = -\frac{1}{\rho}\frac{\partial \overline{P}}{\partial \overline{x}} - \frac{1}{\rho}\frac{\partial p}{\partial x} + \text{SGS}, \quad (9)$$

$$\frac{\partial v}{\partial t} + \mathbf{u}\cdot\nabla v = -\frac{1}{\rho}\frac{\partial p}{\partial y} + \text{SGS}, \quad (10)$$

$$\frac{\partial w}{\partial t} + \mathbf{u}\cdot\nabla w = -g\frac{\rho'}{\rho} - \frac{1}{\rho}\frac{\partial p}{\partial z} + \text{SGS}, \quad (11)$$

$$\frac{\partial S}{\partial t} + \mathbf{u}\cdot\nabla S + u\frac{\partial \overline{S}}{\partial x} = \text{SGS}. \quad (12)$$

If we assume that $(\partial\overline{u}/\partial\overline{x})L_x < u$, where L_x is the box length in the downstream direction, that is, the variation of longitudinal velocity in the along-channel direction is much smaller than the baroclinic velocity itself, we then recover (1)–(4). In the depth-integrated momentum equation for the along-stream velocity [cf. Eq. (1)], there is a three-way balance between the time tendency, the tidal pressure gradient, and the bottom stress. Even though the tidal turbulence is in quasi-equilibrium, the time-tendency term is an important contributor to the momentum balance for the depth-averaged flow (see Li et al. 2005b). If the bottom stress exhibits a flood–ebb asymmetry, the depth-integrated momentum balance will be affected. Hence the tidally averaged volume transport may deviate from zero slightly, leading to a slow trend in the depth-averaged salinity. This deficiency is related to the scale-separation assumption made for deriving the local LES equations. As long as the model integration time is relatively short (a few tidal cycles), the error is small. We will discuss this issue further in section 4.

Because of a high Reynolds number in the flows, we use an approximate bottom boundary condition or a wall layer model. Following Moeng (1984), we specify a bottom stress using a drag law of

$$\frac{\tau}{\rho} = -\overline{u'w'} = C_d u\,|u|\,|_{z=\Delta z/2}, \quad (13)$$

where the drag coefficient is calculated from

$$C_d = \frac{u_*^2}{\overline{u}^2|_{z=\Delta z/2}} = \frac{k^2}{\left[\log\dfrac{\Delta z/2}{z_0}\right]^2}, \quad (14)$$

with z_0 being the roughness height and $k = 0.4$ being the von Kármán constant. For a roughness height of $z_0 = 1$ mm, the drag coefficient is $C_d = 0.0069$ for the velocity at 0.125 m (first grid) above the bottom boundary. Piomelli and Balaras (2002) reviewed wall layer models for LES and concluded that the simple model based on the law of the wall works well in flows over a flat boundary. The subgrid parameterization in our LES model is based on the structure function of Metais and Lesieur (1992).

Since the large-scale forcing is incorporated directly into the governing equations, we can use periodic boundary conditions in the horizontal directions. At the surface, we impose a rigid-lid boundary condition with zero stress. As discussed in Li et al. (2005b), we shall choose a horizontal domain size of 40 m × 40 m and a depth of 10 m, with a uniform grid spacing of 0.25 m and a time step ranging between 0.1 and 0.5 s.

3. Flood–ebb asymmetry in a partially mixed estuary

To better understand mechanisms responsible for generating the tidal asymmetry, we apply the LES model to an idealized partially mixed estuary with a bilinear salinity distribution given by

$$S(x, z) = \left(\frac{\partial \overline{S}}{\partial \overline{x}}\right)(\overline{x} - L) - \frac{N^2}{g\beta}z, \quad (15)$$

where $\partial\overline{S}/\partial\overline{x}$ is the large-scale horizontal salinity gradient and N is the buoyancy frequency measuring the strength of the initial vertical stratification. Assuming a level of no motion at the middepth of the estuarine channel, $z = -H/2$, we can calculate the sea level slope needed to balance the baroclinic pressure gradient; that is,

$$\eta(x) = -\left(\frac{\partial \overline{S}}{\partial \overline{x}}\right)\frac{\beta H}{2}x. \quad (16)$$

Substituting (15) and (16) into (5), we obtain for the longitudinal pressure gradient

$$-\frac{1}{\rho}\frac{\partial P}{\partial x} = F_{\text{tide}} + \left(\frac{\partial \overline{S}}{\partial \overline{x}}\right)g\beta\left(z + \frac{H}{2}\right). \quad (17)$$

We conducted an LES in which the tidal current has a maximum speed of 0.5 m s^{-1} and an M_2 frequency, the water depth is 10 m, and the bottom roughness height is 1 mm. The model was initialized from a state of rest in linearly stratified water. Using typical values found in the Hudson River estuary (cf. Geyer et al. 2000), we took

$$N^2 = -\beta g\frac{dS}{dz} = 7.7\times10^{-4}\times 9.8\times\frac{3}{10} = 2.26\times10^{-3}\ \text{s}^{-2}, \quad (18)$$

$$\frac{\partial \overline{S}}{\partial x} = -2\times10^{-4}\ \text{psu m}^{-1}. \quad (19)$$

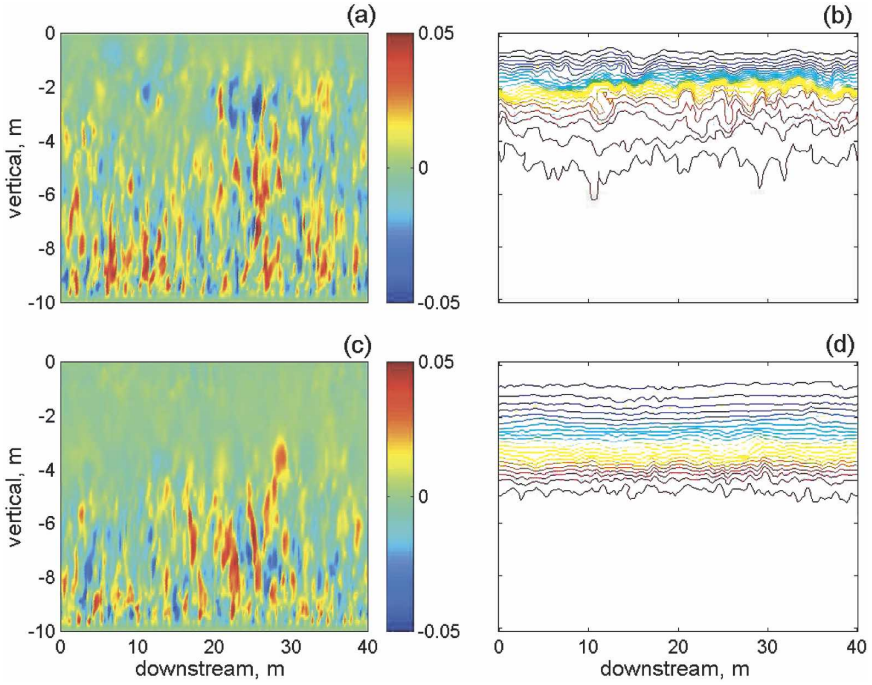

FIG. 2. Comparison of turbulence fields between (top) ebb and (bottom) flood tides in an LES of a partially mixed estuary. Distributions of (a),(c) vertical velocity (m s^{-1}) and (b),(d) salinity (psu) in a vertical section aligned in the along-stream direction.

The LES model produces three-dimensional turbulence fields. In Fig. 2 we plot distributions of vertical velocity and salinity in an along-stream vertical section and compare turbulence characteristics between the peak flood and ebb tides. An energetic turbulent bottom layer is capped by a stratified surface layer at both flood and ebb tides, but the boundary layer penetrates significantly higher during the ebb tide. On flood, isopycnals are almost flat in the stratified region (Fig. 2d). However, on ebb, isopycnals experience large displacements above the bottom boundary layer. In particular, the isopycnals at water depths between 2 and 4 m show localized overturns reminiscent of Kelvin–Helmholtz billows (Fig. 2b). Figure 2 reveals significant differences in turbulence characteristics between the flood and ebb tides. Turbulence in the bottom boundary layer appears to be driven by the bottom friction during the flood tide whereas localized shear-induced turbulence dominates in the outer part of the boundary layer during the ebb tide.

In Figs. 3a,d we examine vertical profiles of the mean salinity and current velocity. At any instant, we define the mean salinity and velocity to be the horizontal averages of salinity and velocity fields, respectively. Turbulent fluctuations are departures from these horizontal averages. The mean salinity profiles show a well-mixed bottom boundary layer at both flood and ebb tides. On flood, a sharp lid caps the boundary layer, and on ebb the bottom boundary layer is thicker and salinity decreases gradually with height (Fig. 3d). The mean velocity at the flood tide shows a subsurface maximum, whereas it appears to be a linear profile at the ebb tide (Fig. 3a). Such a flood–ebb asymmetry in the mean flow profile has been reported in observations (e.g., Nepf and Geyer 1996). As shown in Eqs. (5) and (17), the longitudinal pressure gradient consists of a tidally reversing barotropic part and a nontidal part. The nontidal pressure gradient changes signs from the seaward direction in a surface layer to the landward direction in a bottom layer. On flood, the nontidal pressure gradient reinforces the tidal pressure gradient at depth, such that shear in the mean velocity is reduced everywhere but at the bottom and opposes it near the surface, thus causing the velocity to drop as the water surface is approached. On ebb, the nontidal pressure gradient works in concert with the tidal pressure in the surface layer but opposes it in the bottom layer. This has resulted in a nearly linear distribution of the mean velocity in the vertical direction. Rather than being amplified near the bottom boundary, velocity shear is more or less uniform throughout the water column, creating an environment for shear-induced turbulent mixing at the top of the bottom boundary layer.

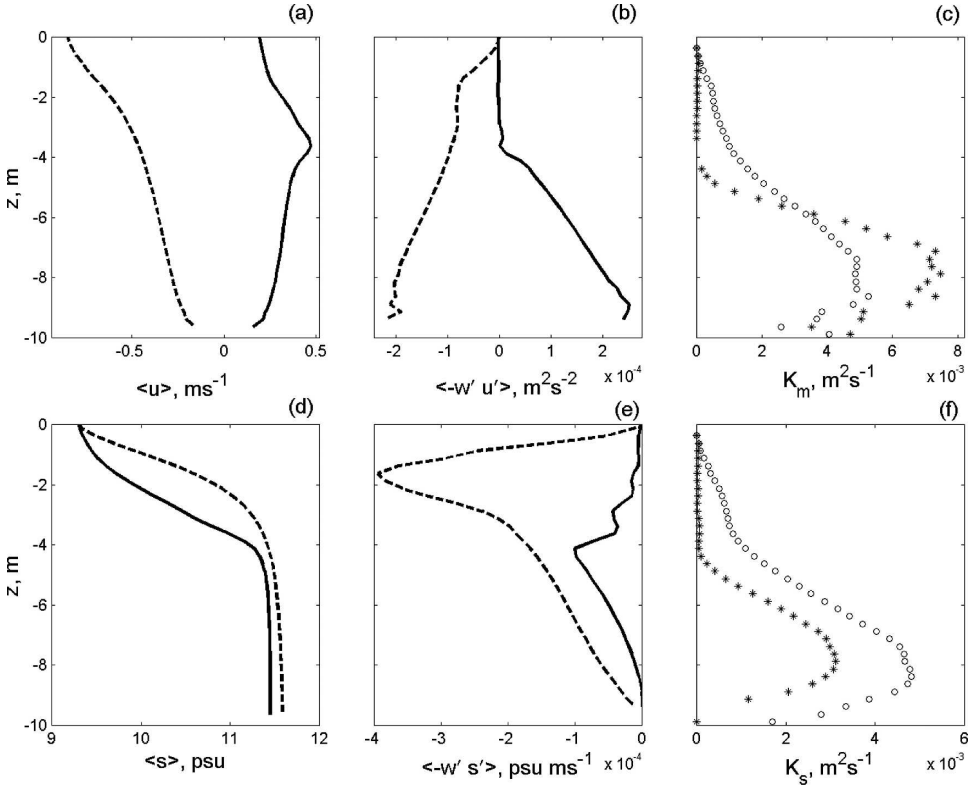

FIG. 3. Vertical profiles of (a) mean velocity, (b) momentum flux, (c) eddy viscosity, (d) mean salinity, (e) salt flux, and (f) eddy diffusivity at peak flood (solid lines or cross symbols) and peak ebb (dashed lines or open circles) tides.

Next we examine vertical momentum and salt fluxes. They are calculated as the horizontal averages of the products of turbulent velocity and salinity fluctuations. We also average them over a 10-min window to obtain more robust statistics. On the flood tide, Reynolds stress decreases linearly with height and falls to zero in the top 4 m where turbulence is suppressed by stratification (Fig. 3b). On the ebb tide, Reynolds stress remains significant in the overturning region (2–4 m) and drops to zero in the top 1–2 m. Geyer et al. (2000) inferred Reynolds stress in the water column from a vertical integral of the momentum equation and also reported a linear decrease with height. Because the nontidal pressure gradient reinforces the tidal pressure gradient at depth on flood but opposes it on ebb, the bottom stress is higher on the flood tide than on the ebb tide, as shown in Fig. 3b. As shown in Fig. 3e, the salt flux increases almost linearly from the bed and reaches a maximum at a middepth. The salt flux on ebb is 4 times as large as that on flood and penetrates much higher in the water column. The predicted salt fluxes agree with those obtained by Peters and Bokhorst (2001). The observed salt fluxes show a middepth maximum between 2×10^{-4} and 4×10^{-4} J kg^{-1} m^{-2} s^{-1}, which is in the same range as shown in Fig. 3e. Large salt fluxes were observed through much of the water column during spring ebbs. Similarly, Fig. 3e shows that large salt flux penetrates nearly to the surface on the ebb tide. To infer turbulent momentum and salt fluxes from dissipation measurements, Peters and Bokhorst (2001) used a model of the flux Richardson number and found sensitivities to some parameters. Therefore the direct flux estimate from LES provides an independent check on the flux estimate from the microstructure measurements.

Using LES outputs, we can obtain a direct estimate of eddy viscosity by calculating the ratio of momentum flux to the mean velocity gradient. Figure 3c shows a parabolic shape within the bottom boundary layer. The maximum eddy viscosity reaches between 0.004 and 0.008 m^2 s^{-1}, which is in the range reported in Geyer et al. (2000) and Peters and Bokhorst (2001). The maximum viscosity on flood is nearly twice as much as that on ebb. This flood–ebb asymmetry is in agreement with Geyer et al. (2000). Inside the bottom boundary layer, the Reynolds stress is higher but the shear in the mean velocity is lower on the flood tide. Although neither the stress increase nor the shear reduction is large, their

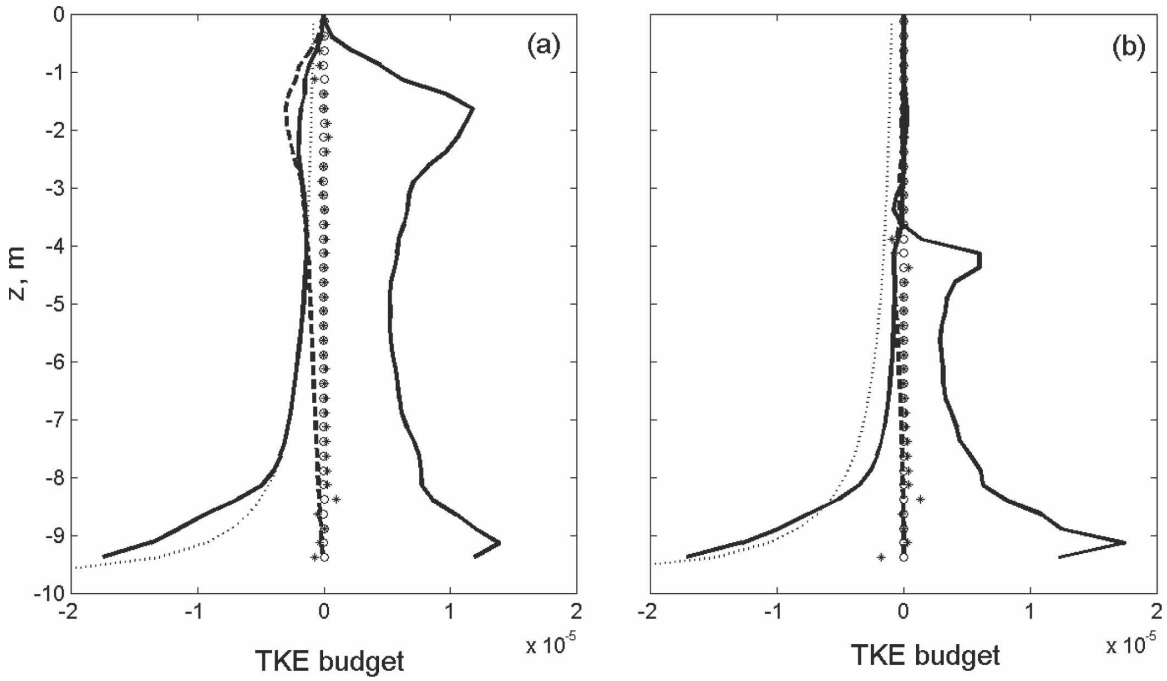

FIG. 4. Vertical profiles of shear production (solid and positive), buoyancy production (dashed), turbulent transport (crosses), pressure transport (open circle), subgrid-scale dissipation (solid and negative), and dissipation rate expected from the law of wall scaling (dotted) at peak (a) ebb and (b) flood tides.

combination results in significant increase in the eddy viscosity, as shown in Fig. 3c. Similarly we can infer eddy diffusivity by calculating the ratio of turbulent salt flux to mean salinity gradient. Because of the larger salt flux, the eddy diffusivity on ebb exceeds that on flood by about 40% (Fig. 3f). If we calculate a turbulent Prandtl number (Pr) as the ratio of the eddy viscosity to the eddy diffusivity, we find that Pr is about 2 on flood but about 1 on ebb. Turbulence closure models (e.g., Burchard and Bolding 2001) and laboratory experiments (e.g., Rohr 1985) suggest that Pr increases with Ri for Ri $>$ ¼, but there is a large scatter for Ri $<$ ¼. In the flood and ebb flows of the LES model, Ri is less than or equal to ¼ inside the bottom boundary layer (see Figs. 5b,e). A value of Pr = 1 on ebb lies within the range obtained from the laboratory experiments (Rohr 1985), but a value of Pr = 2 on flood is higher than the reported range.

To better understand the tidal asymmetry, we examine the horizontally averaged TKE equation

$$\frac{\partial}{\partial t}\left(\overline{\frac{1}{2}q'^2}\right) = \underbrace{-\overline{u'w'}\frac{\partial \overline{U}}{\partial z}}_{\text{S}} \underbrace{-\beta g\overline{w'S'}}_{\text{B}} \underbrace{-\frac{1}{\rho}\overline{\frac{\partial w'p'}{\partial z}}}_{\text{P}} \underbrace{-\frac{\partial}{\partial \mathbf{x}}\overline{\left(\frac{1}{2}q'^2\mathbf{v}'\right)}}_{\text{T}} \underbrace{-\varepsilon}_{\text{D}}, \tag{20}$$

in which terms on the right-hand side of Eq. (20) are referred to as shear production, buoyancy production, pressure transport, turbulent transport, and dissipation, respectively. In Figs. 4a,b, we plot the vertical profiles of TKE terms near the peak flood and peak ebb tides. It was thought that turbulent transport could play an important role in transferring near-bottom turbulent energy to higher levels. However, both pressure and turbulent transport terms calculated from LES are small. This result is consistent with that found in the shear-driven planetary boundary layer. Moeng and Sullivan (1994) compared the shear- and buoyancy-driven planetary boundary layer flows and found that the turbulent and pressure transport terms are negligible in the shear-driven turbulence but do make significant contributions to the TKE budget in the convective turbulence.

Based on near-bottom turbulence measurements in the Hudson River estuary, Trowbridge et al. (1999) reported a production–dissipation balance in the TKE budget and a consistency with the law of wall scaling within 1 m of the seafloor during the flood tides. The

microstructure measurement by Peters and Bokhorst (2000) also showed that the observed dissipation rates correlated well with that expected from the law of wall scaling within 1–2 m of the bottom boundary but departed from it higher in the water column. In Fig. 4 the subgrid scale dissipation calculated from the LES model is compared with the dissipation rate expected from the law of wall scaling ($u_*^3/\kappa z$). A general consistency between the two is found near the bottom. The LES model also shows an approximate production–dissipation balance in the lowest 2 m.

Significant differences can be seen in the vertical profiles of the turbulent shear production term between the flood and ebb tides. On the flood tide, shear production decays rather rapidly away from the bottom boundary, although it shows a secondary peak at the top of the boundary layer (Fig. 4b). In contrast, on the ebb tide, shear production appears to be relatively uniform throughout the boundary layer (Fig. 4a), consistent with the appearance of Kelvin–Helmholtz billows. Because an approximate logarithmic wall layer model is used at the bottom boundary, there is both a slight reduction of Reynolds stress in the lowest two grid points (Fig. 3b) and a possible underestimation of turbulence shear production (Fig. 4). The second peak in shear production reflects increased shear in the zone of increased stratification. However, its size is possibly too large and is an indication that the LES model is losing resolution in the strongly stratified pycnocline region. This overestimation of the shear production term in the outer part of the boundary layer results in a small residual in the depth-integrated TKE budget. Increasing the vertical grid resolution will reduce the error but will not completely eliminate it because the turbulent eddy sizes decrease in the stratified region and will fall below the grid size somewhere. This problem is similar to the resolution issue near the bottom boundary where extremely high resolution would be required to resolve the small turbulent eddies. To address the deficiency near the solid boundary, wall layer models have been developed for the LES models (Piomelli and Balaras 2002). It is possible that finer resolutions and more sophisticated designs of SGS models will also lead to improved simulations of the stratified pycnocline region in the future.

Another difference between the flood and ebb tides is the magnitude of the buoyancy production term. On flood it is practically zero everywhere. However, on ebb it is negative and becomes a significant term in the TKE budget in the outer part of the boundary layer. The negative buoyancy production indicates energy consumption through an increase in the potential energy of the water column by mixing. The ratio of the buoyancy production to the shear production is the flux Richardson number, R_f, which can be interpreted as a measure of the effectiveness of turbulent mixing in increasing the potential energy of the water column. We have used the LES data to calculate this quantity (see Figs. 5a,d). We found that $R_f \approx 0.2$ over a significant fraction of the boundary layer (between 2 and 6 m) at the ebb tide. In contrast, R_f is significantly less than 0.2 inside the boundary layer at the flood tide. Therefore, during the ebb tide a larger fraction of the turbulence shear production is spent on the buoyancy production and less is converted to energy dissipation. This is consistent with a smaller eddy viscosity on the ebb. Further insights can be gained by examining the vertical profile of the gradient Richardson number. On the ebb tide, Ri remains close to the critical value of ¼ over a large portion (between 2 and 6 m deep) of the boundary layer except near the bed (Fig. 5b). In contrast, on the flood tide, Ri increases steadily and reaches the critical value at the edge of the boundary layer (Fig. 5e). The vertical profiles of R_f and Ri reveal a systematic difference in turbulence characteristics between the flood and ebb tides. On the flood tides, turbulence in the bottom boundary layer is primarily driven by the bottom stress, with low R_f and Ri values. On the ebb tides, however, turbulence is generated by both the bottom stress and the local shear, with $R_f = 0.2$ and Ri = ¼ reaching their respective critical values in the outer half of the boundary layer. Peters and Bokhorst (2001) suggested that the flux Richardson number should increase with the gradient Richardson number. Indeed, Fig. 5 shows that R_f increases with Ri and reaches about 0.2 when Ri = ¼.

As mentioned earlier, the LES model loses accuracy in the stratified region above the bottom boundary, causing the flood current to have a vertical profile more pointed than that observed. In the stratified pycnocline region, the outer turbulence scale is substantially diminished. In Figs. 5c,f, we plot the vertical profiles of the buoyancy length scale $L_b = \sigma_w/N$, where σ_w is the root-mean-square of vertical turbulence intensity and N is the buoyancy frequency. Here, L_b is the largest vertical scale in the stratified turbulence. The figures show that $\Delta z < L_b$ within 6 m above the bed on ebb and within 5 m above the bed on flood. Above those heights, the turbulence length scale begins to fall below the grid size, indicating that the LES begins to lose resolution in the outer part of the bottom boundary layer.

4. Strain-induced periodic stratification

In continental shelf regions influenced by freshwater inflows [e.g., the Rhine outflow area of the North Sea

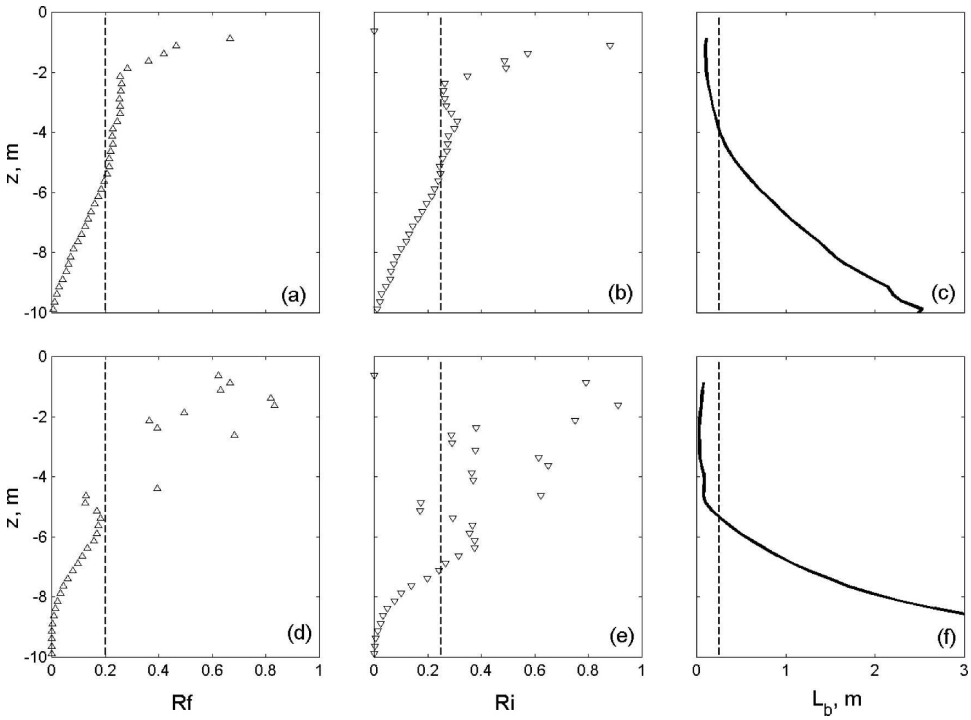

FIG. 5. Vertical profiles of (a),(d) flux and (b),(e) gradient Richardson numbers at peak (top) ebb and (bottom) flood tides. Comparison of turbulence buoyancy scale (solid) with the grid size (dashed) of the LES model at peak (c) ebb and (f) flood tides.

(Simpson and Souza 1995) and the Liverpool Bay (Rippeth et al. 2001], the water column switches between the stratified and mixed states over a single tidal cycle. The LES model is now used to examine this strain-induced periodic stratification. Since the stratification is weak (with the top-to-bottom salinity difference less than 0.5 psu in the model runs explored), the LES results presented in this section do not suffer from the resolution issue discussed in the last section. Our first goal is to test S90's energetics criterion based on the competition between tidal straining and tidal stirring, and Stacey et al. (2001)'s criterion based on the horizontal Richardson number Ri_x. Our second goal is to examine if the strain-induced buoyancy flux makes a significant contribution to turbulence generation on flood tides, as suggested by Stacey and Ralston (2005).

S90 articulated a mechanism by which the horizontal density gradient interacts with vertical shear in the tidal flow to induce periodic stratification at the M_2 frequency. Complete vertical mixing may occur during periods when the contribution of the straining acts to destabilize the water column, followed by periods of stratification when the vertical shear stratifies the water column. S90 developed an elegant, energetic argument for the development of the periodic stratification. In particular, they exploited the scalar quantity

$$\phi = \frac{1}{H}\int_{-H}^{0} (\bar{\rho} - \rho) g z \, dz, \tag{21}$$

which is the amount of work required to bring about complete mixing in the water column. In Eq. (21), H is the water depth, ρ is the density, and $\bar{\rho}$ is the depth-averaged density. By comparing the average input over the ebb half cycle due to tidal straining with the mean tidal stirring power over the same period, S90 derived a criterion for the onset of SIPS. To compare S90 theory with LES results, we define a dimensionless number that may be called a Simpson number:

$$S_x = \frac{\dfrac{2}{\pi} \times 0.031 g H V_{\max} \dfrac{\partial \rho}{\partial x}}{\varepsilon \dfrac{4}{3\pi} C_D \rho \dfrac{V_{\max}^3}{H}}. \tag{22}$$

According to S90, SIPS would occur if $S_x > 1$. Here $\partial\rho/\partial x$ is the horizontal density gradient, ε is the efficiency of tidal mixing, C_D is the effective bottom drag coefficient, g is the gravitational constant, and $V_{\max}$ is the maximum tidal current speed. When estimating the tidal mixing power, S90 assumed $C_D = 2.5 \times 10^{-3}$ and used an empirical value of $\varepsilon = 0.004$, which was determined from the distribution of thermal stratification in

shelf seas. When estimating the amount of work due to tidal straining, S90 made use of an empirical parabolic velocity profile. Although the energetic argument is robust and physically sound, the use of empirical coefficients and velocity profiles warrants an independent check on (24).

Stacey et al. (2001) proposed a horizontal Richardson number to examine the local balance between the stratifying and destratifying forces at the tidal time scale

$$\mathrm{Ri}_x = \frac{g\beta H^2 \partial S/\partial x}{u_*^2}, \tag{23}$$

where β is the saline contraction coefficient and u_* is the bottom frictional velocity. They suggested that Ri_x is a valuable parameter for predicting the onset of residual-creating events. If Ri_x exceeds a threshold value of about 3 on ebb tides, stratification force will overcome tidal stirring force.

We can show that S_x is related to Ri_x by using the drag law $u_* = \sqrt{C_D} V_{\max}$ and a linear equation of state $\rho = \rho_0(1 - \alpha T + \beta S)$, where α is the thermal expansion coefficient. Assuming that the density stratification is dominated by salinity difference, we can rewrite (22) as

$$S_x = \frac{0.092}{2\varepsilon} \frac{g\beta H^2 \partial S/\partial x}{u_*^2} = \frac{0.092}{2\varepsilon} \mathrm{Ri}_x, \tag{24}$$

in which u_* is the friction velocity corresponding to the maximum tidal–current speed. According to S90, SIPS would occur if

$$\mathrm{Ri}_x > \frac{2\varepsilon}{0.092} \approx 0.1 \tag{25}$$

and if the mixing efficiency $\varepsilon = 0.004$. This threshold value is much smaller than 3 suggested by Stacey et al. (2001). If the friction velocity is assumed to vary sinusoidally over the tidal cycle, then (25) may be rewritten as

$$\overline{\mathrm{Ri}_x} > 0.2, \tag{26}$$

where $\overline{\mathrm{Ri}_x}$ is the tidally averaged value of Ri_x. In other words, tidal straining will lead to periodic restratification if the tidally averaged horizontal Richardson number exceeds about 0.2. The paper by Stacey and Ralston (2005) gave the expression

$$\frac{h_{\mathrm{bbl}}}{H} = \left(\frac{R_f}{\mathrm{Ri}_x}\right)^{1/2}, \tag{27}$$

where h_{bbl} is the height of the bottom boundary layer. For a value of R_f at about 0.2, the critical value of Ri_x for full water column mixing should be 0.2. Therefore, the criterion of (26) is consistent with the interpretation that if $\mathrm{Ri}_x > 0.2$, then turbulent mixing will not reach the top of the water column and, consequently, there will be an increase in stratification.

The LES model can be used to test these criteria. To simplify the modeling analysis, we started from a homogeneous water column and switched on tidal currents and a horizontal density gradient. We conducted a number of model runs with different S_x or Ri_x values. To begin, we present results from a model run with the following parameters: water depth $H = 10$ m; the maximum tidal–current speed $V_{\max} = 0.5\ \mathrm{m\ s^{-1}}$; and the horizontal salinity gradient $\partial S/\partial x = 1.5 \times 10^{-4}$, which corresponds to $S_x = 2.11$ if we assume that $C_D = 2.5 \times 10^{-3}$ and $\varepsilon = 0.004$ as suggested in S90. The roughness height was fixed at 3 mm. The horizontal Richardson number depends on the friction velocity, which will be estimated from the turbulence-resolving LES model.

We show the time–depth distributions of mean salinity and current velocity over three tidal cycles in Figs. 6a,b. As expected, velocity profiles show alternating flood and ebb currents. While the ebb velocity shows a monotonic increase with height, the flood velocity is more uniformly distributed. Because of mixing, salinity contours are aligned vertically during flood tides, indicating no vertical stratification. As freshwater is brought over saltwater during ebb tides, the water column becomes stratified. In Fig. 6c we plot the time–depth distribution of the horizontally averaged TKE, which shows a flood–ebb asymmetry: it is larger and penetrates higher on floods than on ebbs. The energy dissipation rate also shows a tidal asymmetry that is less pronounced than that of TKE.

When examining density and current profiles collected in an estuarine channel in the San Francisco Bay, Stacey and Ralston (2005) found negative gradient Richardson numbers and unstable density profiles in the upper portions of the boundary layer during the flood tides. Based on these results, they suggested that the tidal asymmetry is due to the strain-induced buoyancy flux, which is stabilizing on ebb tides but destabilizing on flood tides. Figures 7a,b show the vertical profiles of turbulent salt flux calculated from the LES model. In agreement with Stacey and Ralston (2005), the salt flux is negative on ebb but switches to the positive sign on flood, indicating the development of convective turbulence. Will this unstable buoyancy flux promote turbulence generation on the flood tides? To answer this question, we compare the shear production with the buoyancy production. As shown in Figs. 7c,d, the shear production greatly exceeds the buoyancy production during both flood and ebb tides. Therefore, the strain-induced negative buoyancy flux on the flood tide does

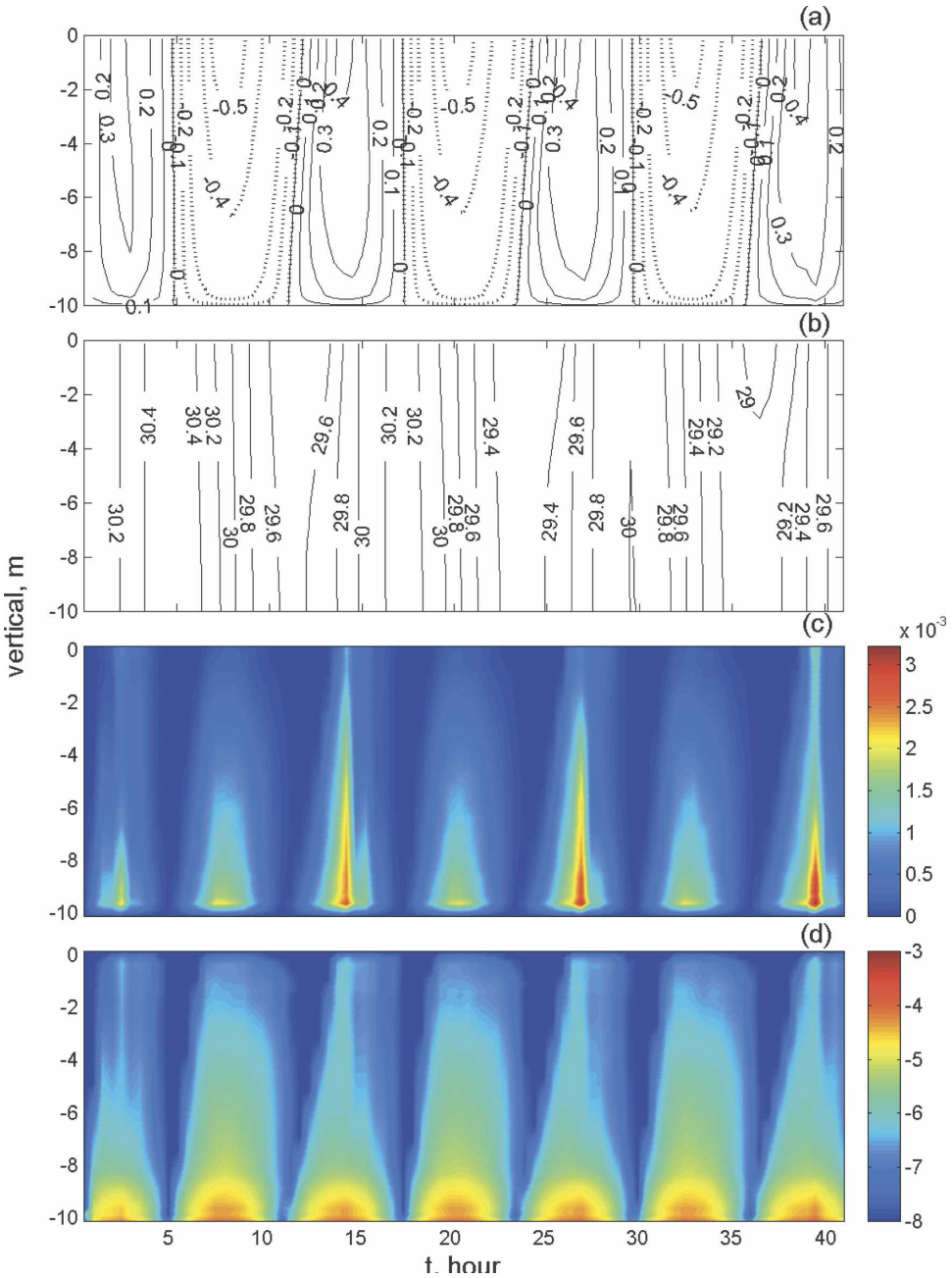

FIG. 6. Evolution of mean and turbulent fields over three tidal cycles in an LES run of SIPS: (a) mean velocity (m s^{-1}), (b) mean salinity (psu), (c) horizontally averaged TKE (m^2 s^{-2}), and (d) the logarithm of the horizontally averaged dissipation rate (m^2 s^{-3}).

not make a significant contribution to turbulence generation and cannot explain the enhanced mixing on the flood.

In the next two figures we investigate the time series of some flow diagnostics over tidal cycles. The depth-averaged current shows a sinusoidal fluctuation, as expected in an oscillating tidal flow (Fig. 8b). The bottom friction velocity also shows a nearly sinusoidal fluctuation, although it is slightly larger at the peak flood than at the peak ebb (Fig. 8a). In Fig. 8c, we plot the time series of the depth-integrated TKE, which fluctuates at the M_4 frequency. The turbulence field gets charged during flood or ebb tides but discharged during the slack phases. It is interesting to note that the maximum TKE obtained at the peak floods is twice as large as that obtained at the peak ebbs. Hence turbulence in-

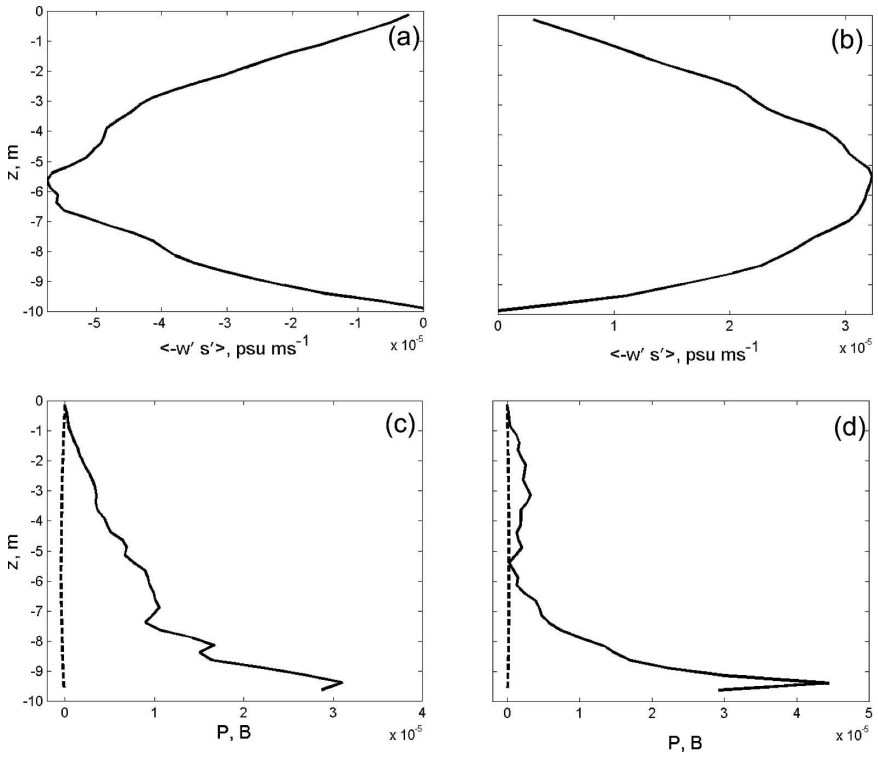

FIG. 7. Vertical profiles of (a),(b) salt flux and (c),(d) shear production (solid) and buoyancy production (dashed) at peak (left) ebb and (right) flood tides.

tensity is stronger on floods than on ebbs, which is a manifestation of the flood–ebb asymmetry. In Fig. 8d, we plot the time series of depth-integrated turbulence shear production, buoyancy production, and subgrid-scale dissipation. Except in an initial spinup period, the dominant balance in the depth-integrated TKE budget is between the shear production and dissipation. The buoyancy production remains small throughout the tidal cycles, confirming that the negative buoyancy flux produced during the flood tides does not play a major role in generating turbulence in the water column.

Time series of the depth-averaged salinity and top-to-bottom salinity difference are shown in Figs. 9a,b. As discussed in section 2, the depth-averaged salinity shows a long-term decreasing trend because of the slight asymmetry in bottom stress, but this should not affect the results reported here. The differential salt advection by the vertically sheared current, or the tidal straining, produces fluctuations in stratification. Indeed, there is a periodic switching between the stratified and well-mixed conditions. It is interesting to notice the two stratification peaks within each tidal cycle. Stratification starts to build up during the ebb tide and reaches a small peak in early ebb. As the ebb current gains in strength and generates turbulent mixing, stratification is reduced somewhat. However, tidal straining subsequently overwhelms tidal stirring, leading to increasing stratification that continues into the flood tide. The peak stratification is actually found at about 1.5 h after the initiation of the flood tide (see Fig. 9b). This time delay is expected, because most of the water column still has a shear in the stratifying direction until the flood boundary layer extends past the middle of the water column. Strong turbulent mixing generated by the flood tide ultimately erases the stratification, as shown by the rapid decent in ΔS during the middle part of the flood tide. The stratification then hovers around zero before picking up again in the ebb phase. The whole cycle of destratification and restratification repeats for the three tidal cycles that the LES model simulated. We calculated the buoyancy deficit ϕ as defined in (21). Since it is an integrated measure of the salinity difference from the vertical average, ϕ shows a similar time history as that of the vertical salinity difference.

Stacey et al. (2001) suggested that the horizontal Richardson number is a dimensionless quantity that determines the onset of residual flow and restratification events. We plot Ri_x in Fig. 9d and find that it exceeds the threshold value of 3 only during the slack tides when the bottom stress is very small. The horizontal Richardson number does not rise above 3 during the

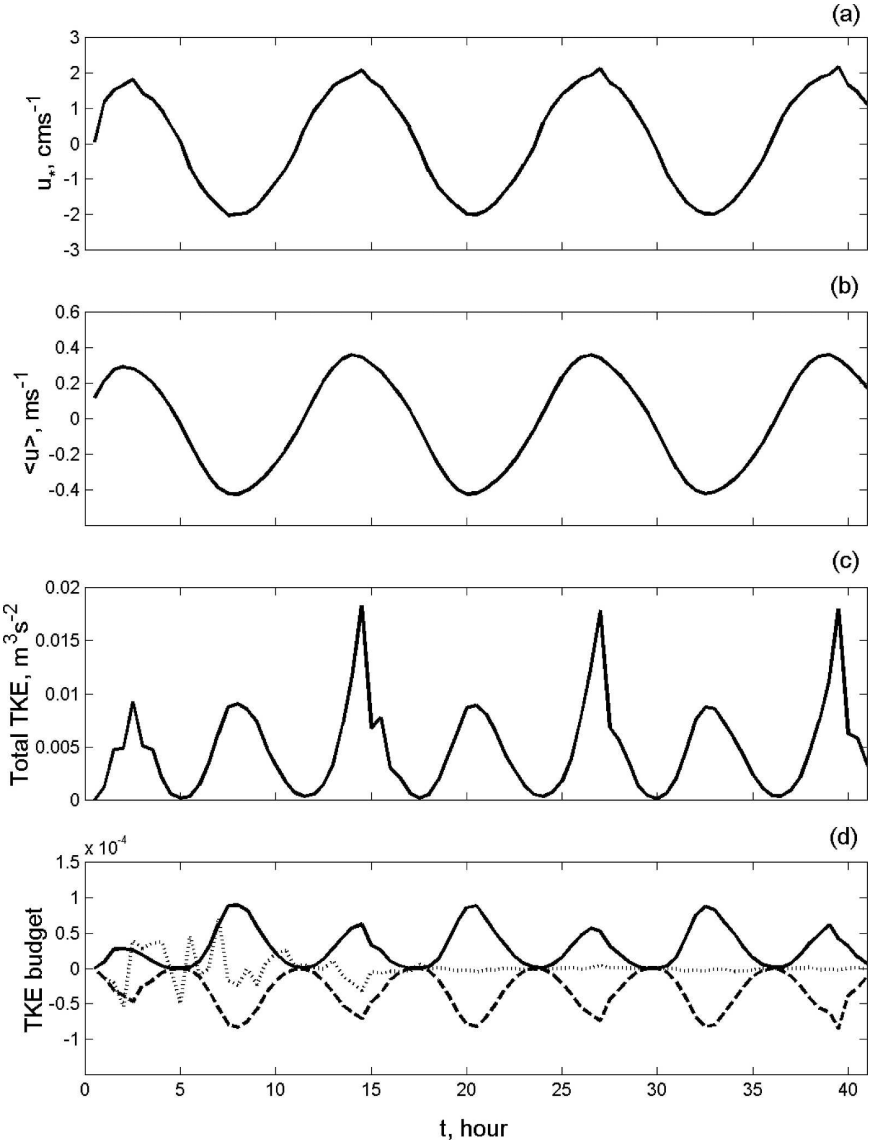

FIG. 8. Time series of (a) friction velocity, (b) depth-averaged velocity, (c) depth-integrated TKE, and (d) depth-integrated shear production (solid), dissipation (dashed), and buoyancy production (dotted).

ebb tides when stratification is built up in the water column. Although the instantaneous value of Ri_x can be useful for detecting "episodes" of exchange flow within a tidal cycle, we think that the tidally averaged $\overline{\mathrm{Ri}_x}$ is more appropriate for determining the onset of stratification here. By using the time history of the bottom friction velocity, we found $\overline{\mathrm{Ri}_x} = 0.57$. This is larger than the threshold value of about 0.2 in (26) so that the periodic stratification shown in the LES results is expected by the theoretical criterion.

We conducted a number of LES runs to explore the parameter space. These were separated into three groups: in the first, we fixed $V_{\max} = 0.5\ \mathrm{m\ s^{-1}}$ and $H = 10$ m but varied $\partial S/\partial x$ over a significant range $(8 \times 10^{-5},\ 1.2 \times 10^{-4},\ 1.5 \times 10^{-4},\ 2 \times 10^{-4})\ \mathrm{psu^{-1}}$, which corresponds to $S_x = (1.12,\ 1.68,\ 2.11,\ 2.81)$ if we use $C_D = 2.5 \times 10^{-3}$ and $\varepsilon = 0.004$. These runs are denoted as "baroclinic cases." In the second, we turned off the nontidal pressure gradient term [the second and third terms in Eq. (5)] in the momentum equation but kept the straining of the salinity field [first term on the right-hand side of Eq. (4)] in the salinity equation. We fixed $V_{\max} = 0.5\ \mathrm{m\ s^{-1}}$ and $H = 10$ m but varied $\partial S/\partial x = (1.0 \times 10^{-4},\ 1.5 \times 10^{-4},\ 2.0 \times 10^{-4})\ \mathrm{psu^{-1}}$. These runs are denoted as "barotropic cases." In the third, to simulate deeper shelf water, we used a box size of 40 $\times$

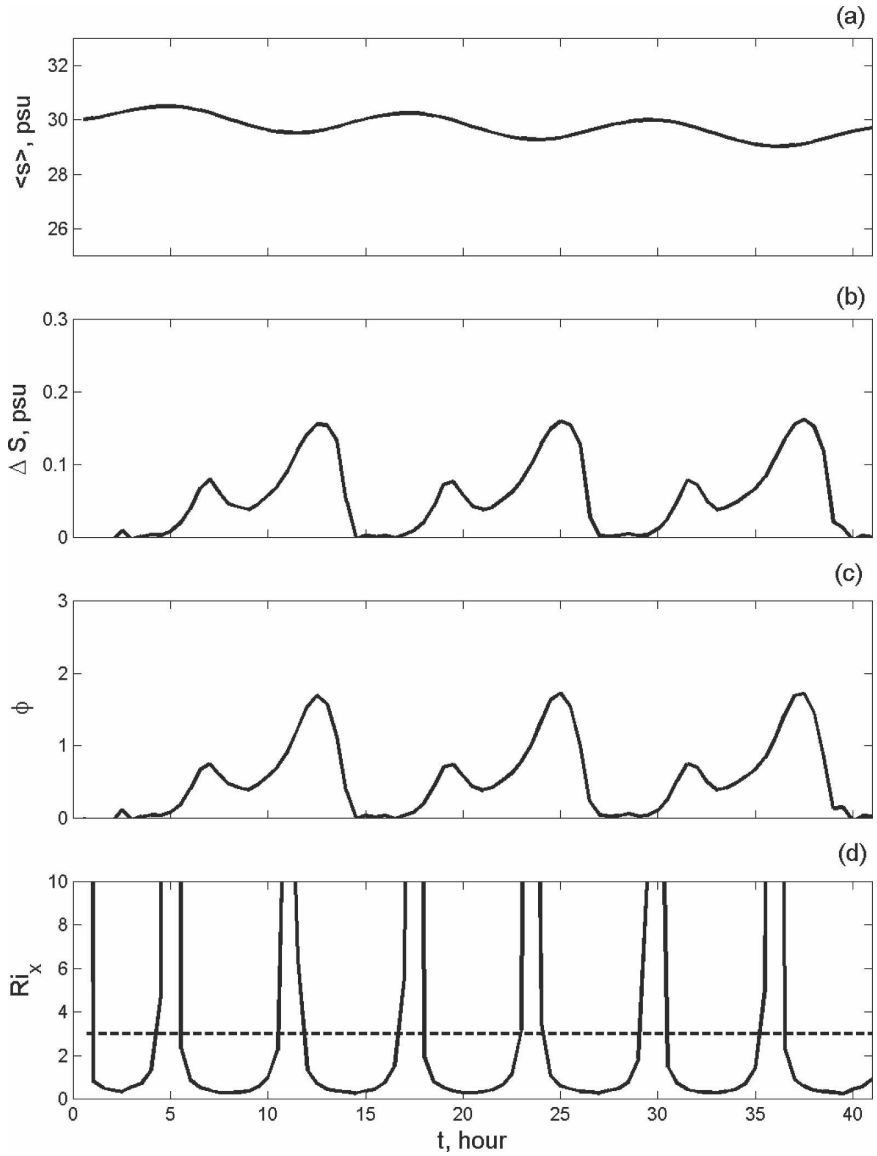

FIG. 9. Time series of (a) depth-averaged salinity, (b) top–bottom salinity difference, (c) buoyancy deficit, and (d) the horizontal Richardson number.

160 × 160 m and a grid size of 1 m. The nontidal pressure gradient was retained in these calculations. The maximum tidal current speed was set at $V_{\max} = 1.0\ \mathrm{m\ s^{-1}}$ and the water depth $H = 40$ m. We denote these runs as "shelf cases." We chose a coarser resolution for the shelf case because of the constraint of the computing power. However, based on our experience with the upper-ocean LES (Li et al. 2005a), a 1-m grid size should be sufficient to resolve turbulent eddies in such weakly stratified water.

To summarize the results from these LES runs, we calculate the top-to-bottom salinity difference (ΔS), including the tidally averaged stratification $\overline{\Delta S}$ and the maximum stratification $\Delta S_{\max}$ during a tidal cycle. We examine how they vary with the Simpson number S_x and the tidally averaged horizontal Richardson number $\overline{\mathrm{Ri}_x}$. As shown in Fig. 10a, the tidally averaged $\overline{\Delta S}$ increases with S_x and $\overline{\Delta S}$ is negligible for $S_x < 1$. Hence S90's energetics criterion is accurate in predicting the onset of SIPS events. In Fig. 10b, we examine how $\overline{\Delta S}$ and $\Delta S_{\max}$ vary with $\overline{\mathrm{Ri}_x}$. There is more scatter in the maximum stratification because it is averaged over only two or three values obtained from the model runs. The theoretical threshold (26) is marked in the figure for comparison. Although neither the averaged nor the maximum stratification shows an abrupt jump across

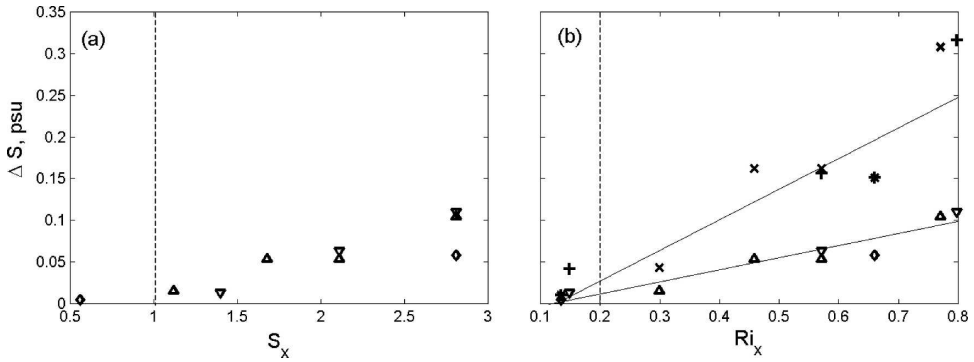

FIG. 10. Stratification (the top–bottom salinity difference) as functions of (a) Simpson number S_x and (b) tidally averaged horizontal Richardson number $\overline{\mathrm{Ri}_x}$ for different LES runs. Symbols are defined as follows: tidally averaged stratification for baroclinic (up triangle), barotropic (down triangle), and shelf (diamond) cases; maximum stratification for baroclinic (x), barotropic (+), and shelf cases (cross).

$\overline{\mathrm{Ri}_x} = 0.2$, significant stratification is only established for $\overline{\mathrm{Ri}_x} \geq 0.3$. The tidally averaged stratification $\overline{\Delta S}$ is very small for the two runs with $\overline{\mathrm{Ri}_x} < 0.2$. Figure 10b shows that both $\overline{\Delta S}$ and $\Delta S_{\max}$ increase with $\overline{\mathrm{Ri}_x}$. In the model runs reported here, the stratification builds up during a part of the tidal cycle but is destroyed during the remaining part of the tidal cycle. However, as $\overline{\mathrm{Ri}_x}$ increases, the duration of complete destratification gets shorter, lasting for about 1 h at $\overline{\mathrm{Ri}_x} = 0.8$. It is expected that permanent stratification may be established for $\overline{\mathrm{Ri}_x} > 1$. We have also examined how the peak flood–ebb TKE ratio varies with $\overline{\mathrm{Ri}_x}$ and found that the ratio increases from about 1 to about 3 as $\overline{\mathrm{Ri}_x}$ increases from 0.1 to 0.8, but it contains large scatter due to the same reason as for the maximum stratification.

The flood–ebb mixing asymmetry can be caused by the flood–ebb asymmetry in bed stress and by the tidal straining of the density field. To evaluate the relative roles of the baroclinic pressure gradient and the tidal straining of the salinity field, we compare the results from the first and second group of LES runs. As mentioned earlier, the baroclinic pressure gradient was switched off in the momentum equation in the second group of numerical experiments. No significant differences are detected in $\overline{\Delta S}$ (up triangles versus down triangles) and $\Delta S_{\max}$ (x marks versus + symbols) values between the two groups of model runs (Fig. 10b). This suggests that the tidal straining of the salinity field is the main contributor to the flood–ebb tidal asymmetry. It was somewhat surprising to find that the baroclinic term remains insignificant at $\mathrm{Ri}_x = 0.8$, although this result is consistent with Stacey et al. (2001) and Burchard and Baumart (1998). Furthermore, no systematic differences are detected for the third group of runs, which have water depths of 40 m and a maximum current speed of 1 m s^{-1}, confirming that the box size does not affect the model results.

In agreement with the results presented in Figs. 7c,d and 8d, we found that the depth-integrated buoyancy production is less than 5% of the integrated shear production in all model runs, suggesting that the strain-induced buoyancy flux does not make a substantial contribution to turbulence generation during the flood tides. This result disagrees with Stacey and Ralston (2005) but is consistent with Li et al. (2005a), who investigated the transition from shear- to buoyancy-driven turbulence in the ocean surface mixed layer. They found that the transition occurs at $H/(-L) \approx 4.5$, where H is the mixed layer depth and $L = -u_*^3/(\kappa B_0)$ is the Monin–Obukhov length. Following Stacey and Ralston (2005), we may estimate the strain-induced buoyancy flux as

$$B_0 = \beta g \left(\frac{u_*}{\kappa}\right) \frac{\partial S}{\partial x} H. \tag{28}$$

Substituting (28) into the definition of the Monin–Obukhov length, one gets

$$\frac{H}{-L} = \frac{\beta g \dfrac{\partial S}{\partial x} H^2}{u_*^2} = \mathrm{Ri}_x. \tag{29}$$

According to Li et al. (2005a), the transition from the shear to convective turbulence occurs at $\mathrm{Ri}_x = H/(-L) \approx 4.5$. For typical values of tidal currents and the horizontal density gradient found in estuaries and shelf regions, as exemplified in the above LES runs, $\overline{\mathrm{Ri}_x}$ is generally less than 1. Therefore, it seems unlikely that the buoyancy flux will contribute much to turbulence generation on flood tides. Consequently, the flows do not switch from shear- to buoyancy-driven turbulence over the ebb–flood tidal cycle.

5. Conclusions

Using an LES model, we investigated how the horizontal density gradient affects the dynamics of tidal bottom boundary layer in both stratified and weakly stratified water. We examined the turbulent kinetic energy budget and found that the primary balance is between the shear production and dissipation. Turbulent and pressure transport terms were negligible and did not play a significant role in transporting turbulent energy away from the bottom boundary. We also found that the strain-induced buoyancy production is small. Although the salt flux switches sign over a tidal cycle, the turbulence flow does not change from the shear-driven turbulence on the ebb tides to buoyancy-driven turbulence on the flood tides. This result differs from Stacey and Ralston (2005)'s suggestion that the tidal asymmetry is due to the strain-induced buoyancy flux.

We have reconciled the energetics criterion based on the competition between tidal straining and tidal stirring with the empirical criterion based on the horizontal Richardson number Ri_x. We showed that tidal straining will lead to periodic stratification when the tidally averaged $\overline{\mathrm{Ri}_x} > 0.2$, which is lower than the 3 suggested in Stacey et al. (2001). By comparing with the LES results on the transition from the shear- to buoyancy-driven turbulence in the ocean surface mixed layer, we propose that the strain-induced buoyancy flux will become important in generating turbulence on the flood tides when $\overline{\mathrm{Ri}_x} > 4.5$. However, $\overline{\mathrm{Ri}_x} < 1$ for typical values of the horizontal density gradient and tidal currents found in estuaries and for shelf regions influenced by lateral freshwater inputs. Hence we conclude that turbulence generation will be dominated by the shear production.

Despite its limitation in the stratified pycnocline and its pressing demand on the computing power, we believe that the LES model is a promising tool for unraveling the intricate physics in stratified shear flows found in estuaries and coastal oceans. The small spatial scales of the turbulent eddies and the extreme anisotropy of the outer scales of flow make stratified turbulence a challenging problem to simulate numerically. This paper represents a first step toward developing an LES model that can be applied to turbulent mixing processes in estuaries and shelf seas. The novel contribution is the explicit consideration of the large-scale density gradient, which has not been considered in previous LES simulations of geophysical boundary layers. In future investigations, we plan to use finer resolution, to run LES in parallel machines, and to exploit the use of dynamic eddy viscosity models. We hope that the new LES model under development will provide more accurate simulations of the entrainment processes. We also plan to run the LES model over spring–neap tidal cycles and compare it with a wealth of observational data collected in the Hudson River or other estuaries. This would require refining the local LES equations to incorporate the larger-scale adjustments in the baroclinic pressure field.

Besides serving as a useful tool for understanding turbulent mixing processes, LES can be used to test and improve turbulence closure models used in regional ocean models. Turbulence closure remains a significant impediment to accurate numerical simulations, particularly in the presence of stable stratification (e.g., Li et al. 2005c). The high-resolution turbulence data obtained from LES can be used to test, evaluate, and refine turbulence parameterization schemes and improve the predictions of regional ocean models.

Acknowledgments. We thank two referees for their helpful comments. This work is supported by Grants OCE-0451699 and OCE-0451740 from the National Science Foundation.

REFERENCES

Brown, A. R., S. H. Derbyshire, and P. J. Mason, 1994: Large-eddy simulation of stable atmospheric boundary layers with a revised stochastic subgrid model. *Quart. J. Roy. Meteor. Soc.,* **120,** 1485–1512.

Burchard, H., and H. Baumart, 1998: The formation of estuarine turbidity maxima due to density effects in the salt wedge. A hydrodynamic process study. *J. Phys. Oceanogr.,* **28,** 309–321.

——, and K. Bolding, 2001: Comparative analysis of four second-moment turbulence closure models for the oceanic mixed layer. *J. Phys. Oceanogr.,* **31,** 1943–1968.

Geyer, W. R., J. H. Trowbridge, and M. M. Bowen, 2000: The dynamics of a partially mixed estuary. *J. Phys. Oceanogr.,* **30,** 2035–2048.

Jay, D. A., and J. D. Smith, 1990: Residual circulation in shallow estuaries. 2. Weakly stratified and partially mixed, narrow estuaries. *J. Geophys. Res.,* **95,** 733–748.

Li, M., C. Garrett, and E. Skyllingstad, 2005a: A regime diagram for classifying turbulent large eddies in the upper ocean. *Deep-Sea Res. I,* **52,** 259–278.

——, L. Sanford, and S.-Y. Chao, 2005b: Time-dependent effects in unstratified tidal flows: Results from large eddy simulations. *Estuarine Coastal Shelf Sci.,* **62,** 193–204.

——, L. Zhong, and W. C. Boicourt, 2005c: Simulations of Chesapeake Bay estuary: Sensitivity to turbulence mixing parameterizations and comparison with observations. *J. Geophys. Res.,* **110,** C12004, doi:10.1029/2004JC002585.

Mason, P. J., and S. H. Derbyshire, 1990: Large-eddy simulation of the stably-stratified atmospheric boundary layer. *Bound.-Layer Meteor.,* **53,** 117–162.

Metais, O., and M. Lesieur, 1992: Spectral large-eddy simulations of isotropic and stably-stratified turbulence. *J. Fluid Mech.,* **239,** 157–194.

Moeng, C.-H., 1984: A large-eddy simulation model for the study of planetary boundary-layer turbulence. *J. Atmos. Sci.,* **41,** 2052–2062.

——, and P. P. Sullivan, 1994: A comparison between shear- and buoyancy-driven planetary boundary layer flows. *J. Atmos. Sci.,* **51,** 999–1022.

Nepf, H. M., and W. R. Geyer, 1996: Intratidal variations in stratification and mixing in the Hudson estuary. *J. Geophys. Res.,* **101,** 12 079–12 086.

Peters, H., 1999: Spatial and temporal variability of turbulent mixing in an estuary. *J. Mar. Res.,* **57,** 805–845.

——, and R. Bokhorst, 2000: Microstructure observations of turbulent mixing in a partially mixed estuary. Part I: Dissipation rate. *J. Phys. Oceanogr.,* **30,** 1232–1244.

——, and ——, 2001: Microstructure observations of turbulent mixing in a partially mixed estuary. Part II: Salt flux and stress. *J. Phys. Oceanogr.,* **31,** 1105–1119.

Piomelli, U., and E. Balaras, 2002: Wall-layer models for large-eddy simulations. *Annu. Rev. Fluid Mech.,* **34,** 349–374.

Pritchard, D. W., 1956: The dynamic structure of a coastal plain estuary. *J. Mar. Res.,* **15,** 33–42.

Rippeth, T. P., N. R. Fisher, and J. H. Simpson, 2001: The cycle of turbulent dissipation in the presence of tidal straining. *J. Phys. Oceanogr.,* **31,** 2458–2471.

Rohr, J. J., 1985. An experimental study of evolving turbulence in uniform mean shear flow with and without stable stratification. Ph.D. dissertation, University of San Diego, 271 pp.

Simpson, J. H., and A. J. Souza, 1995: Semidiurnal switching of stratification in the region of freshwater influence of the Rhine. *J. Geophys. Res.,* **100,** 7037–7044.

——, J. Brown, J. Matthews, and G. Allen, 1990: Tidal straining, density currents, and stirring the control of estuarine stratification. *Estuaries,* **13,** 125–132.

——, H. Burchard, N. R. Fisher, and T. P. Rippeth, 2002: The semi-diurnal cycle of dissipation in a ROFI: Model-measurement comparisons. *Cont. Shelf Res.,* **22,** 1615–1628.

Skyllingstad, E. D., W. D. Smyth, J. N. Moum, and H. Wijesekera, 1999: Upper-ocean turbulence during a westerly wind burst: A comparison of large-eddy simulation results and microstructure measurements. *J. Phys. Oceanogr.,* **29,** 5–28.

Stacey, M. T., and D. K. Ralston, 2005: The scaling and structure of the estuarine bottom boundary layer. *J. Phys. Oceanogr.,* **35,** 55–71.

——, J. R. Burau, and S. G. Monismith, 2001: Creation of residual flows in a partially stratified estuary. *J. Geophys. Res.,* **106,** 17 013–17 043.

Trowbridge, J. H., W. R. Geyer, M. M. Bowen, and A. J. Williams III, 1999: Near-bottom turbulence measurements in a partially mixed estuary: Turbulent energy balance, velocity structure, and along-channel momentum balance. *J. Phys. Oceanogr.,* **29,** 3056–3072.

Wang, D., J. C. McWilliams, and W. G. Large, 1998: Large-eddy simulation of the diurnal cycle of deep equatorial turbulence. *J. Phys. Oceanogr.,* **28,** 129–148.